analytica

MDPI

Article

Intrinsic Calix[6]arene Fluorescence for Quantitative Characterization of Group I and Group II Metal Cation Complexation

Andrea Usenik [1,*], Franka Sunjka [1], Karla Kukina Gradečak [1], Luka Klemen [1], Katarina Leko [1], Nikola Cindro [1], Gordan Horvat [1], Ivo Piantanida [2] and Vladislav Tomišić [1,*]

[1] Department of Chemistry, University of Zagreb Faculty of Science, Horvatovac 102A, HR-10000 Zagreb, Croatia; fsunjka.chem@pmf.hr (F.S.); kkukinagradecak.chem@pmf.hr (K.K.G.); lklemen.chem@pmf.hr (L.K.); kleko@chem.pmf.hr (K.L.); ncindro@chem.pmf.hr (N.C.); ghorvat@chem.pmf.hr (G.H.)

[2] Division of Organic Chemistry and Biochemistry, Ruđer Bošković Institute, Bijenička Cesta 54, HR-10000 Zagreb, Croatia; ivo.piantanida@irb.hr

* Correspondence: ausenik.chem@pmf.hr (A.U.); vtomisic@chem.pmf.hr (V.T.)

Abstract

Calixarenes lacking additionally introduced fluorophores have long been considered insufficiently fluorescent for fluorimetric sensing. We have recently shown that simple calix[4]arene derivatives possess weak intrinsic fluorescence which significantly changes upon cation binding, raising a question whether the same holds for their larger and more flexible analogs. The aim of this work was to investigate the intrinsic fluorescence of the tertiary-amide calix[6]arene derivative **L** and to establish whether the changes accompanying complexation can be used for quantitative characterization of alkali and alkaline earth metal cation complexation. Stability constants of the 1:1 and 2:1 (cation:ligand) complexes in acetonitrile were determined by spectrofluorimetric titrations and validated by UV absorption spectrophotometry and isothermal titration calorimetry. Compared with the latter techniques, fluorimetry could be performed at much lower receptor concentrations, in some cases in the micromolar range. Complex stoichiometries and structures were further examined by NMR spectroscopy, mass spectrometry, and molecular dynamics simulations. Although **L** contains no additional fluorophore, it exhibits relatively weak intrinsic fluorescence which is strongly affected by cation binding. Among the alkali metal ions, pronounced fluorescence enhancement was observed for K^+ and to a slightly lesser extent Rb^+, whereas Li^+ and Cs^+ caused fluorescence quenching. Sodium ions induced both effects, depending on concentration. In contrast, all alkaline earth metal cations reduced the fluorescence intensity. The emission changes were interpreted in terms of variations in the absorption spectra and conformational rigidification upon complexation, as well as possible suppression of the photoinduced electron transfer and involvement of charge-transfer character of the excited state. Fluorimetry based on the intrinsic fluorescence of **L** proved superior to absorption spectrophotometry and microcalorimetry for the quantitative characterization of complexation reactions, offering a valuable advantage for poorly soluble systems and highly stable complexes.

Keywords: calixarenes; fluorescence; sensing; metal cations; complexation; stability constants

Check for updates

Academic Editor: Marcello Locatelli

Received: 4 August 2026
Revised: 23 September 2026
Accepted: 24 September 2026
Published: 29 September 2026

Copyright: © 2026 by the authors. Licensee MDPI, Basel, Switzerland. This article is an open access article distributed under the terms and conditions of the Creative Commons Attribution (CC BY) license.

1. Introduction

Calixarenes are an important class of macrocyclic compounds that have been studied extensively because their structures can be tailored to bind a wide range of ions and neutral molecules [1–5]. Owing to this versatility, calixarene derivatives have found use in numerous areas, particularly in sensing [6–13], extraction [14–18], functional materials [19–22], and catalysis [23,24]. Over the past decade, they have increasingly been employed in medicinal [25–30], pharmaceutical [31–34], and biological applications [9,33,35–37].

The binding ability of calixarenes is governed by several factors, including the type of the donor groups, the characteristics of the binding cavity, the size and charge of the guest, and the solvent used [38–45]. Derivatives bearing oxygen-donor groups at the lower rim, such as amides, esters, or ketones, are well known to strongly bind high-charge-density metal cations, including alkali and alkaline earth metal cations [14,38–40,46,47]. Tertiary-amide derivatives are especially attractive receptors due to the high basicity of the corresponding carbonyl oxygen atoms [14,39,46,48,49]. Among calixarenes of different ring sizes, calix[6]arenes are of particular interest because their relatively large cavity can accommodate larger cations. In addition, their greater conformational flexibility compared with smaller homologues gives rise to complexes of various stoichiometries [49–53].

Fluorimetry is especially useful for binding studies as it permits detection at much lower concentrations than other commonly used techniques (e.g., spectrophotometry, NMR spectroscopy, or titration calorimetry). This reduces the amount of receptor required, which is especially advantageous in the cases of poor solubility, and allows the determination of high equilibrium constants that are difficult to access by less sensitive methods [54].

Fluorescent calixarene receptors have typically been obtained by attaching fluorophores to the calixarene backbone, which itself has long been considered as "non-fluorescent" [4]. Recently, however, we found that simple calix[4]arene derivatives lacking an appended fluorophore display intrinsic fluorescence that changes markedly upon cation complexation [10]. This finding raised several questions: whether the same property is also characteristic of related compounds such as the larger calix[6]arenes, how the intrinsic fluorescence depends on the size of the calixarene and the charge density of the bound cation, and whether it could be used both to discriminate between cations and to determine high stability constants by direct titrations at low working concentrations [10]. To the best of our knowledge, the only related report is the paper by Tranfić Bakić et al. [55], in which the fluorescence of amide and ester calix[6]arene derivatives was examined for studying the complexation of lanthanide cations in acetonitrile. However, the authors concluded that the fluorescence of the calixarenes was insufficient for this purpose and that the cation-binding-induced changes in the emission properties of the receptors were insignificant.

Nevertheless, in the present work we examined the intrinsic fluorescence of the calix[6]arene diethylamide derivative **L** (Figure 1), a compound of interest both for its cation-complexation ability [49,52] and because the larger calixarene macrocycles remain far less studied than their calix[4]arene analogs. Although cation binding by such compounds has been characterized by a variety of techniques [49,52,55,56], their intrinsic emission properties have not been exploited. The aim of this study was therefore to explore the fluorescence of **L** and to assess whether monitoring its changes upon complexation with alkali and alkaline earth metal cations could serve as a quantitative method for evaluating the binding characteristics of the ligand. To compare the fluorescence of **L** with that of its parent lower-rim unsubstituted compound, the analogous calix[4]arene derivative, and the monomer constituting the calixarene derivatives, the corresponding fluorescence quantum yields were assessed. The values of complex stability constants determined by means of spectrofluorimetric titrations were verified by comparison with those obtained using absorption spectrophotometry and isothermal titration calorimetry. In addition, NMR

spectroscopy, mass spectrometry, and molecular dynamics simulations were employed to provide insight into the complex structures, as well as to elucidate the effect of cation binding on the conformation of the ligand and, consequently, on its fluorescence.

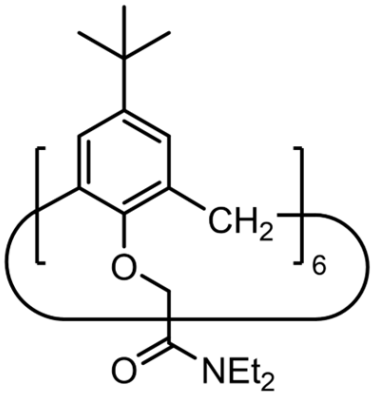


Figure 1. Structure of the investigated calix[6]arene **L**.

2. Materials and Methods

2.1. Materials

Compound **L** was prepared according to the procedure described in ref. [56] from *p-tert*-butylcalix[6]arene (Ajelis, Juvisy, France, for synthesis) which was additionally purified for quantum yield measurements. The monomeric compound was synthesized as described in reference [10].

Acetonitrile (Sigma-Aldrich, Steinheim, Germany, ≥99.0%, HPLC grade) was used as a solvent without additional purification. The salt solutions for complexation studies were prepared by direct weighing and dissolution of the following salts in volumetric flasks: lithium perchlorate (Sigma-Aldrich, Steinheim, Germany, 99.99%), sodium perchlorate (Sigma-Aldrich, Seelze, Germany, ≥98%), potassium perchlorate (Fluka, Buchs, Switzerland, ≥99.0%), rubidium tetraphenylborate ($RbBPh_4$, Sigma-Aldrich, Steinheim, Germany, 95%), rubidium nitrate (Aldrich, Milwaukee, WI, USA, 99.95%), cesium iodide (Merck, Darmstadt, Germany, 99.9%), cesium perchlorate (Sigma-Aldrich, Steinheim, Germany, 99.9%), magnesium perchlorate hexahydrate (Sigma-Aldrich, Steinheim, Germany, 99%), magnesium nitrate hexahydrate (Merck, Darmstadt, Germany, Suprapur®), calcium perchlorate tetrahydrate (Sigma-Aldrich, Steinheim, Germany, 99%), strontium perchlorate trihydrate (Alfa Aesar, Kandel, Germany, >98%), barium perchlorate (Fluka, Buchs, Switzerland, ≥98%), and barium trifluoromethanesulfonate ($Ba(trf)_2$, Sigma-Aldrich, Steinheim, Germany, >98%). Calix[4]arene analog was synthesized according to the procedure described in our previous work [10]. CD_3CN (Eurisotop, Saint-Aubin, France, >99.80% D) was used as a solvent for ^1H NMR experiments. Acetonitrile (Carlo Erba, Milano, Italy, MS grade) was used for preparing the solutions for mass spectrometry experiments, as well as the mobile phase along with water (VWR, Radnor, PA, USA, MS grade).

L-tyrosine (Merck, Darmstadt, Germany, >99%) solution in aqueous phosphate buffer (pH = 7.0, c = 0.02 mol dm^{-3}, prepared from KH_2PO_4 (Kemika, Zagreb, Croatia, *pro analysi*), and $Na_2HPO_4 \times 2\ H_2O$ (Kemika, Zagreb, Croatia, *pro analysi*) in MilliQ water) was used as a standard for quantum yield studies.

2.2. UV-Vis Absorption Spectrometry

Spectrophotometric titrations were carried out by means of UV-Vis spectrophotometers Agilent Cary 5000 and 60 (Agilent, Santa Clara, CA, USA). The solution of ligand **L** (V_0 = 2.2 cm^3 or V_0 = 2.5 cm^3) was titrated with the appropriate salt solution, and the spec-

tra were recorded with a step of 1 nm and an integration time of 0.2 s with baseline correction at ϑ = (25.0 ± 0.1) °C. For spectrophotometric titrations of **L** with Li^+, Na^+, K^+, Rb^+, Cs^+, Mg^{2+}, Ca^{2+}, Sr^{2+} and Ba^{2+} in acetonitrile, the solutions of following concentrations were used: 8.88×10^{-5} to 2.40×10^{-4} mol dm^{-3} (**L**), 1.92×10^{-3} mol dm^{-3} ($LiClO_4$), 2.16×10^{-3} to 2.50×10^{-3} mol dm^{-3} ($NaClO_4$), 1.91×10^{-3} to 2.08×10^{-3} mol dm^{-3} ($KClO_4$), 1.64×10^{-3} mol dm^{-3} ($RbNO_3$), 5.03×10^{-3} mol dm^{-3} ($CsClO_4$), 3.43×10^{-3} mol dm^{-3} ($Mg(NO_3)_2$), 2.43×10^{-3} mol dm^{-3} ($Ca(ClO_4)_2$), 2.08×10^{-3} mol dm^{-3} ($Sr(ClO_4)_2$), and 2.08×10^{-3} mol dm^{-3} ($Ba(trf)_2$). The experiments were carried out in triplicate. The obtained spectrophotometric data were processed using the HypSpec program (version 2.0.0.2) from the HYPERQUAD software package (Protonic Software, Leeds, UK) [57].

2.3. Fluorimetry

Spectrofluorimetric titrations were carried out using an Agilent Cary Eclipse spectrofluorimeter (Agilent, Santa Clara, CA, USA). The solution of **L** (V_0 = 2.5 cm^3) was titrated with the salt solution, and the spectra of the corresponding reaction mixtures were recorded with a step of 2 nm and an integration time of 0.4 s at ϑ = (25.0 ± 0.1) °C. For spectrofluorimetric titrations of **L** with Li^+, Na^+, K^+, Rb^+, Cs^+, Mg^{2+}, Ca^{2+}, Sr^{2+} and Ba^{2+} in acetonitrile, the solutions of following concentrations were used: 1.04×10^{-6} to 1.99×10^{-5} mol dm^{-3} (**L**), 7.52×10^{-4} to 1.92×10^{-3} mol dm^{-3} ($LiClO_4$), 6.73×10^{-4} to 2.23×10^{-3} mol dm^{-3} ($NaClO_4$), 6.99×10^{-4} to 8.11×10^{-4} mol dm^{-3} ($KClO_4$), 1.12×10^{-3} mol dm^{-3} ($RbNO_3$), 1.00×10^{-2} mol dm^{-3} ($CsClO_4$), 4.80×10^{-4} mol dm^{-3} ($Mg(ClO_4)_2$), 9.58×10^{-4} mol dm^{-3} ($Ca(ClO_4)_2$), 8.46×10^{-4} mol dm^{-3} ($Sr(ClO_4)_2$), and 7.44×10^{-4} mol dm^{-3} ($Ba(ClO_4)_2$). The experiments were carried out in triplicate. Overlap between the excitation and emission spectra of the ligand was taken into account during fitting, and the obtained fluorimetric data were processed using the HypSpec program (version 2.0.0.2) from the HYPERQUAD software package (Protonic Software, Leeds, UK) [57].

2.4. Quantum Yield Determination

Fluorescence quantum yields were determined using Agilent Cary Eclipse spectrofluorimeter and Cary 5000 spectrophotometer (Agilent, Santa Clara, CA, USA) according to the procedure described in refs. [58–65]. Experimental details are provided in the Supplementary Materials.

2.5. Isothermal Titration Calorimetry

Microcalorimetric titrations were carried out by means of a Malvern MicroCal VP-ITC microcalorimeter (Worcestershire, UK, V_{cell} = 1.43 cm^3). For titration of **L** with Li^+, Na^+, K^+, Rb^+, Cs^+, Mg^{2+}, Ca^{2+}, Sr^{2+}, and Ba^{2+} in acetonitrile, the solutions of following concentrations were used: 9.71×10^{-5} to 2.04×10^{-4} mol dm^{-3} (**L**), 1.92×10^{-3} mol dm^{-3} ($LiClO_4$), 2.36×10^{-3} mol dm^{-3} ($NaClO_4$), 1.91×10^{-3} mol dm^{-3} ($KClO_4$), 4.74×10^{-3} mol dm^{-3} ($RbBPh_4$), 2.51×10^{-3} mol dm^{-3} (CsI), 1.02×10^{-3} mol dm^{-3} ($Mg(NO_3)_2$), 9.00×10^{-4} to 1.17×10^{-3} mol dm^{-3} ($Ca(ClO_4)_2$), 1.16×10^{-3} to 2.08×10^{-3} mol dm^{-3} ($Sr(ClO_4)_2$) and 1.06×10^{-3} mol dm^{-3} ($Ba(ClO_4)_2$). Experiments were conducted at ϑ = (25.0 ± 0.1) °C by addition of the metal salt solution to the solution of ligand **L** by an automated burette (V = 0.300 cm^3). Thus obtained enthalpy changes were corrected for titrant dilution heats. The experiments were carried out in triplicate, and the data were processed using Microcal OriginPro 7.0 and OriginPro 7.5 (OriginLab Corporation, Northampton, MA, USA) or HypDH program (version 1.1.0.28) from the HYPERQUAD software package (Protonic Software, Leeds, UK) [66].

2.6. Mass Spectrometry

Mass spectrometry experiments were carried out using an Agilent 6550 Series Accurate-Mass-Quadrupole Time-of-Flight (Q-TOF) high-resolution mass spectrometer with direct sample injection using the Agilent 1290 Infinity II HPLC system with electrospray ionization (Agilent, Santa Clara, CA, USA). Sample solutions were introduced into the instrument via direct injection of 2 µL, with mobile phase flow = 0.4 cm^3 min^{-1}. The mobile phase consisted of acetonitrile and water in the ratio 1:1 (*v*/*v*). The mass spectra were recorded in the range of m/z = 100 to m/z = 3200 in positive ion mode. The instrument working conditions were as following: sheath gas temperature = 350 °C, sheath gas flow = 11 dm^3 min^{-1}, nebulizer pressure = 35 psi, capillary potential = 4 kV, nozzle voltage = 0 V, drying gas temperature = 225 °C and drying gas flow = 17 dm^3 min^{-1}. Nitrogen was used as sheath and drying gas. The metal salts were added depending on species distribution in acetonitrile and log *K* values as 2, 5, or 10 equivalents. The final concentration of **L** in the solution was ≈1×10^{-5} mol dm^{-3}.

2.7. NMR Studies

^{1}H NMR spectra were recorded on Bruker Avance III HD 400 MHz/54 mm Ascend (5 mm PA BBI 1H/D-BB probe with *z*-gradient and automatic tuning) and Bruker Avance Neo 600 (5 mm Prodigy cryoprobe with *z*-gradient, Rheinstetten, Germany). All proton spectra were obtained based on 16 or 32 scans, using 64K data points, and spectral width of 20 ppm. Solutions of **L** and perchlorate salts were prepared by dissolving the solids in deuterated acetonitrile. The solution of **L** (V_0 = 0.5–0.9 cm^3) was titrated with the perchlorate salt solutions. Spectra were recorded at (25.0 ± 0.1) °C. For the titration of **L** with Li^+, Na^+, K^+, Ca^{2+}, Sr^{2+}, and Ba^{2+}, the solutions of following concentrations were used: 2.57×10^{-4} to 1.01×10^{-3} mol dm^{-3} (**L**), 1.32×10^{-2} mol dm^{-3} ($LiClO_4$), 1.09×10^{-2} mol dm^{-3} ($NaClO_4$), 1.01×10^{-2} mol dm^{-3} ($KClO_4$), 2.40×10^{-2} mol dm^{-3} ($Ca(ClO_4)_2$), 1.03×10^{-2} mol dm^{-3} ($Sr(ClO_4)_2$) and 5.89×10^{-3} mol dm^{-3} ($Ba(ClO_4)_2$).

2.8. MD Simulations

The molecular dynamics simulations were carried out by means of a GROMACS package (version 2026.2, University of Groningen, The Netherlands; Royal Institute of Technology, Uppsala University, Sweden) [67–72]. Intramolecular and nonbonded intermolecular interactions were modeled by the CHARMM36 (Chemistry at HARvard Macromolecular Mechanics) force field [73]. Complex simulations were initiated by placing a cation in the binding-site center between the ether atoms, followed by energy minimization and *NVT* production simulation *in vacuo*. In the case of simulations in solution, the above starting complexes were solvated in a cubical box of 6.5 nm side length previously equilibrated solvent with a periodic boundary condition. An energy minimization procedure was again performed, followed by a 100.5 ns of *NpT* production simulation. Initial velocities were sampled from Maxwell–Boltzmann distribution at 300 K. In the case of calcium complex the simulation time was extended to 200.5 ns due to the slow acetonitrile basket inclusion process. The *v*-rescale thermostat [74] and *c*-rescale barostat [75] were used to maintain constant pressure (1 bar, 2 ps time constant) and temperature (298 K, 0.2 ps time constant) during the simulation. All simulations were performed without replication. First 0.5 ns of production simulation were discarded during data analysis. The system temperature, density and total energy converged to stable values well within first 0.5 ns of simulation time. The integrator used for the propagation and the temperature control was velocity-Verlet algorithm [76] with a time step of 1 fs. Atomic coordinates were saved every 1000 steps. The cutoff radius for nonbonded van der Waals and short-range Coulomb interactions was set to 15 Å. Long-range Coulomb interactions were treated by the Ewald method [77].

Average molecular structures of the complexes were obtained by principal component analysis (PCA) on a coordination matrix whose rows contained distances between the metal cation and ether and carbonyl oxygen atoms. Angles between metal cations and carbonyl groups were also added to the coordination matrix. The chosen structures were closest to the centroids of the most populated clusters in space defined by the first two principal components. Figures of molecular structures were created using VMD software (version 1.9.2, University of Illinois, Champaign, IL, USA) [78].

3. Results and Discussion

3.1. Emission Properties of **L**

The excitation and emission spectra of calix[6]arene **L** in acetonitrile are presented in Figure 2, clearly showing that the compound exhibits intrinsic fluorescence. Upon excitation at the absorption maximum (272 nm), the emission maximum is observed at 308 nm. The excitation and emission spectra show no significant overlap (Stokes shift of 4300 cm^{-1}), similar to that reported previously for the analogous calix[4]arene [10].

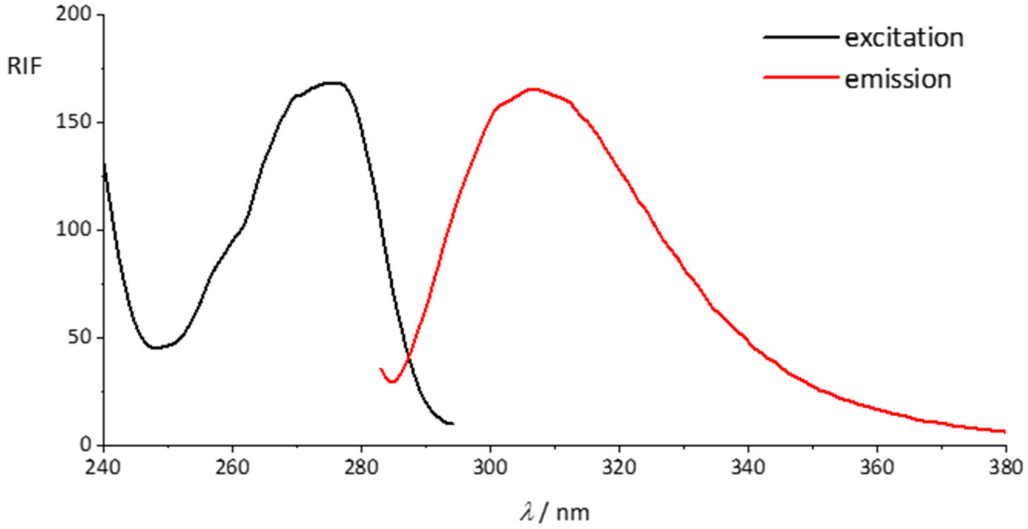


Figure 2. Excitation (λ_{em} = 302 nm) and emission spectra (λ_{exc} = 272 nm) of **L** ($c = 2.0 \times 10^{-5}$ mol dm^{-3}) in MeCN at (25.0 ± 0.1) °C. Excitation slit = 5 nm, emission slit = 10 nm.

Prior to the detailed fluorimetric investigation of the complexation properties of **L**, several experimental parameters needed to be optimized. These included examining the linear range of fluorescence intensity–concentration relationship, assessing possible photodegradation of the compound under irradiation, and adjusting the excitation and emission slit widths to obtain an appropriate fluorescence signal. The dependence of relative intensity of fluorescence (RIF) on the concentration of **L** in acetonitrile is shown in Figure S1. The intensity increases proportionally with concentration up to approximately 2×10^{-5} mol dm^{-3}, beyond which it deviates downwards from linearity (Figure S1), which can be presumably attributed to the inner filter effect. Based on this finding, the initial concentration of **L** used in fluorimetric titrations was in the range of approximately 1×10^{-6} to 2×10^{-5} mol dm^{-3}. Possible photodegradation of **L** was further examined by recording fluorescence spectra upon exposure to a xenon lamp for several hours. A slight decrease in RIF was observed (Figure S2), which was, however, negligible (<2%) over the time period typically required for the titration experiment.

3.2. Cation Complexation with **L**

As examples, spectrofluorimetric titrations of **L** with $NaClO_4$ and $KClO_4$ in acetonitrile are shown in Figures 3 and 4, respectively. Binding of alkali metal cations in acetonitrile resulted in a blue shift in the maximum emission in all cases (Figures 3, 4 and S3–S7), similar to that previously observed for the smaller amide calix[4]arene derivative [10]. However, the changes in the emission spectra upon complexation of first-group cations were much more pronounced and strongly dependent on the bound cation. During the titrations, fluorescence enhancement was observed for K^+ and Rb^+ over the entire concentration range, whereas Na^+ caused an initial decrease in fluorescence intensity up to a Na^+:**L** molar ratio of approximately 1, followed by an increase at higher cation concentrations. In contrast, complexation with Li^+ and Cs^+ resulted in fluorescence quenching over the entire examined cation:**L** molar ratio range. The most remarkable finding of the fluorimetric experiments was the pronounced fluorescence enhancement induced by potassium and rubidium binding (Figures 4 and S4–S6), which allowed the working concentrations to be reduced to 5×10^{-6} or even 1×10^{-6} mol dm^{-3}, approximately two orders of magnitude lower than in the corresponding UV absorption (Figures S10 and S11) and ITC (Figures 5 and S15) titrations.

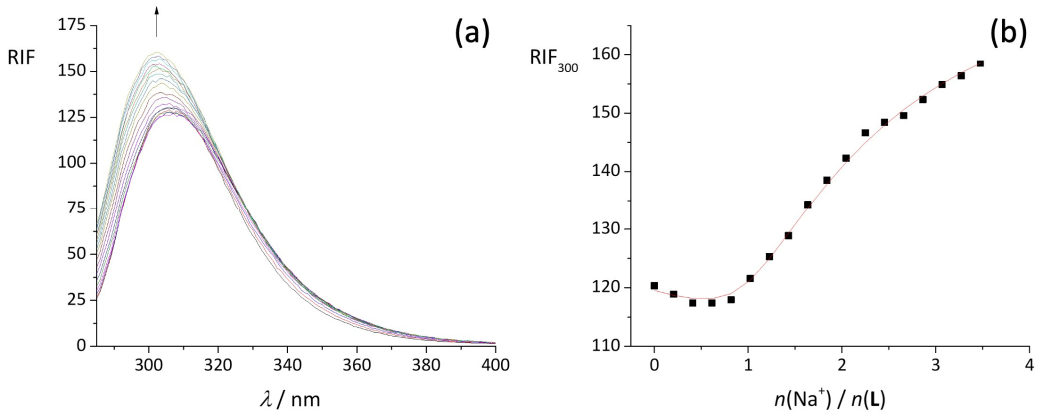


Figure 3. (**a**) Fluorimetric titration of **L** (c = 1.32 × 10^{-5} mol dm^{-3}) with $NaClO_4$ (c = 6.73 × 10^{-4} mol dm^{-3}) in MeCN; ϑ = (25.0 ± 0.1) °C; V_0(**L**) = 2.5 cm^3; λ_{exc} = 272 nm; excitation slit 5 nm, emission slit 10 nm. Spectra are corrected for dilution. (**b**) Dependence of the relative intensity of **L** fluorescence at 300 nm on the cation-to-ligand molar ratio. ■ experimental; – calculated.

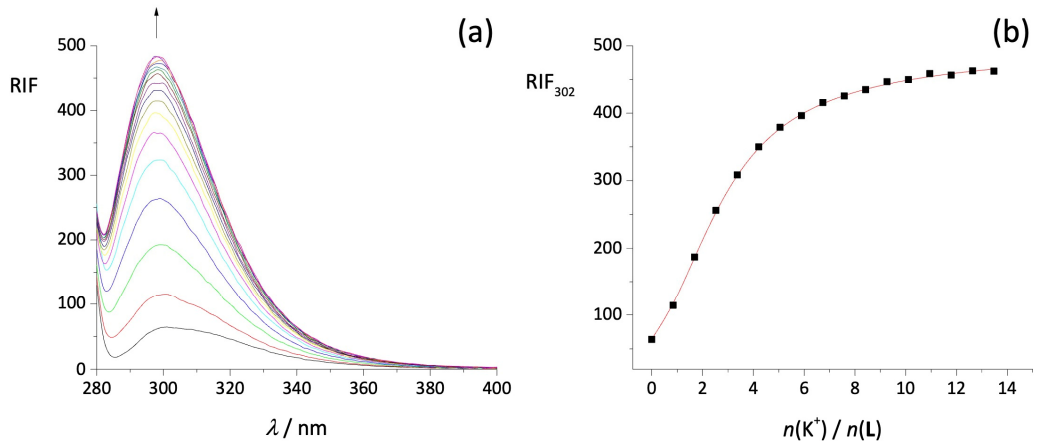


Figure 4. (**a**) Fluorimetric titration of **L** (c = 4.98 × 10^{-6} mol dm^{-3}) with $KClO_4$ (c = 6.99 × 10^{-4} mol dm^{-3}) in MeCN; ϑ = (25.0 ± 0.1) °C; V_0(**L**) = 2.5 cm^3; λ_{exc} = 272 nm; excitation slit 5 nm, emission slit 10 nm. Spectra are corrected for dilution. (**b**) Dependence of the relative intensity of **L** fluorescence at 302 nm on the cation-to-ligand molar ratio. ■ experimental; – calculated.

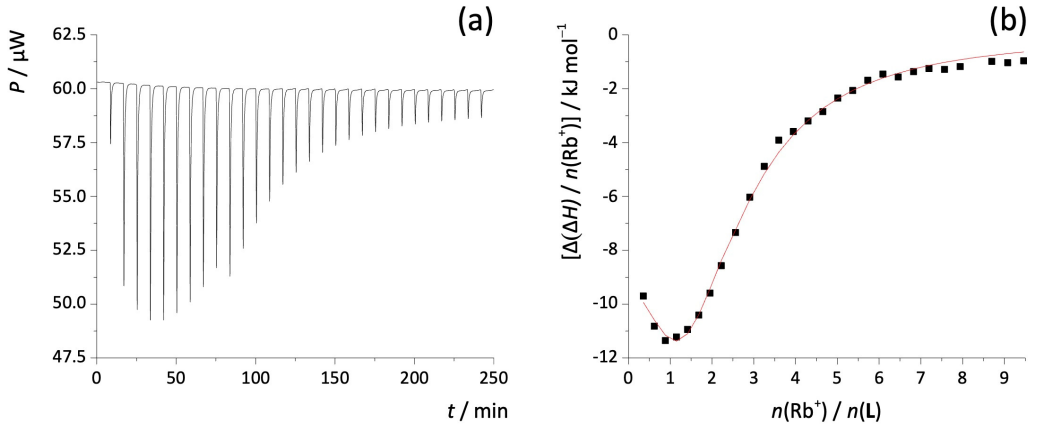


Figure 5. Microcalorimetric titration of **L** (c = 1.02 × 10^{-4} mol dm^{-3}) with $RbBPh_4$ (c = 4.74 × 10^{-3} mol dm^{-3}) in MeCN; ϑ = (25.0 ± 0.1) °C; V(**L**) = 1.43 cm^3. (**a**) Thermogram. (**b**) Dependence of normalized successive enthalpy change on the cation-to-ligand molar ratio. ■ experimental; – calculated.

The sigmoidal shape of the binding isotherms corresponding to K^+ and Rb^+ complexation (Figures 4 and S6), and even more clearly that observed for Na^+ (Figure 3b), suggests the formation of ML^+ and M_2L^{2+} complexes (M denotes alkali metal cation). Accordingly, the titration data were successfully fitted by multivariate nonlinear regression analysis according to the model comprising 1:1 and 2:1 (cation:ligand) complexes, and the same holds for the titrations of **L** with Li^+. Although a signal corresponding to the 2:1 complex with the cesium cation was observed in the related mass spectrum (see next paragraph), satisfactory agreement between the experimental and calculated Cs^+ + **L** titration data was obtained by considering only the formation of the 1:1 complex (Figure S7), in accordance with the results of molecular dynamics simulations (see below). The resulting complex stability constants are listed in Table 1. To validate the obtained values, additional UV absorption (Figures S8–S12) and microcalorimetric (Figures 5 and S13–S16) experiments were performed. Processing of the corresponding titration data confirmed the stoichiometries of the complexes, with the equilibrium constants determined by different methods being in quite good agreement. However, the largest stability constants of Li^+ and Na^+ complexes could be reliably determined only by means of fluorimetry, as their values were too high to be quantified by the other two less sensitive methods (Table 1).

It is worth noting that no supporting electrolyte was added to the working solutions to keep the system as simple as possible. Nevertheless, the possible influence of ionic strength, counterions used in the titrations, and ion-pairing should be taken into account. The obtained results, however, appear to provide an internal test of these effects. For reactions yielding 1:1 complexes, the activity coefficients of the free and complexed metal ions, which have the same charge, can reasonably be assumed to largely cancel out in the stability-constant equation. On the other hand, this consideration does not apply to the formation of 2:1 complexes. Despite this, the values of the equilibrium constants determined by means of different techniques, over a wide range of ligand and cation concentrations, and moreover with anions as different as ClO_4^-, NO_3^-, BPh_4^-, and trf^-, are mutually consistent. If ion-pairing, counterion, or ionic-strength effects were appreciable under the experimental conditions, such agreement would not be expected.

Complex stoichiometries were additionally confirmed by mass spectrometry. As can be seen from the data given in Table S1 and in the spectra shown in Figures S17–S22, for all solutions containing **L** and an alkali metal cation salt, signals at m/z values corresponding to $[\mathbf{L} + M]^+$ and $[\mathbf{L} + 2M]^{2+}$ ions were observed. Furthermore, the signals showed isotopic distribution consistent with the expected composition of the respective ions.

Table 1. Complex stability constants for complexation of **L** with alkali metal cations in acetonitrile at 25 °C. Uncertainty of the last digit, given in parentheses, corresponds to the standard error of the mean (SE, $N = 3$).

Cation	M^+:L	log $K \pm$ SE		
		FLUO	UV	ITC
Li^+	1:1	6.7 (2)	>6 [3]	>6 [3]
	2:1	5.2 (2)		
Na^+	1:1	7.0 (3)	>6 [3]	>6 [3]
	2:1	4.6 (1)		
K^+	1:1	5.3 (2) [1] 5.30 (2) [2]	5.5 (2)	5.5 (1)
	2:1	5.1 (2) [1] 5.17 (3) [2]	5.29 (1)	5.20 (3)
Rb^+	1:1	4.64 (8) [1] 4.1 (2) [2]	4.23 (5)	4.7 (1)
	2:1	4.1 (3) [1] 4.08 (5) [2]	4.49 (5)	3.89 (2)
Cs^+	1:1	4.28 (2)	4.29 (1)	– [4]

[1] Concentration of **L** solution used in titrations $\approx 1 \times 10^{-6}$ mol dm^{-3}. [2] Concentration of **L** solution used in titrations $\approx 5 \times 10^{-6}$ mol dm^{-3}. [3] Roughly estimated, as the values are too large to be reliably determined by direct absorption spectrophotometric or calorimetric titrations. [4] Could not be determined due to $\Delta_r H \approx 0$.

The conformational rigidification of **L**, which affects its fluorescence emission properties (see next section), is expected upon cation binding. That was indeed observed by ^{1}H NMR titrations of the ligand with cations in deuterated acetonitrile. In the proton spectrum of free **L**, most of the signals are rather broad, suggesting its high conformational flexibility. However, the addition of metal ions caused substantial changes in the spectrum (Figures 6, S23 and S24). Namely, all signals became clearly sharper, indicating a reduction of the internal ligand motions. The dependence of spectral changes on cation-to-ligand molar ratio is consistent with the corresponding species distribution diagrams shown in Figures S25–S27. These distributions were calculated based on the stoichiometries and complex stability constants determined fluorimetrically and using the NMR experimental conditions. For alkali metal cations, spectral changes were observed up to the $n(M^+)/n(\mathbf{L})$ ratio of ≈2 (K^+, Figure 6) or somewhat higher values (Na^+ and Li^+, Figures S23 and S24), depending on the thermodynamic stabilities of the corresponding complexes. These findings further support the results obtained by fluorimetry and other techniques.

The data listed in Table 1 show that the stability constants of the 1:1 and 2:1 complexes of **L** with first-group cations span a rather wide range. To provide another quantitative measure of the selectivity of **L**, we use here a conditional selectivity coefficient defined relative to Na^+ as the ratio of the total concentrations of bound cations:

$$S_{Na^+/M^+} = \frac{[NaL^+] + 2[Na_2L^{2+}]}{[ML^+] + 2[M_2L^{2+}]} \quad (1)$$

at constant ligand concentration $c(\mathbf{L}) = 10^{-5}$ mol dm^{-3}, and with $c(Na^+) = c(M^+)$ varied simultaneously. The equilibrium concentrations in Equation (1) were calculated using the corresponding stability constants (Table 1). The variation in this concentration-dependent quantity with analytical metal-ion concentration for different cations is presented in Figure S28. As follows from the corresponding stability constants, the affinities of

L for Na^+ and Li^+ are similar, whereas for the other M^+ cations, the Na^+/M^+ selectivity increases with cation concentration in a cation-size-dependent manner. At the molar ratio $n(Na^+)/n(\mathbf{L}) = n(M^+)/n(\mathbf{L}) = 5$, the selectivity coefficient reaches values of 9 for K^+, ≈900 for Rb^+, and ≈1300 for Cs^+.

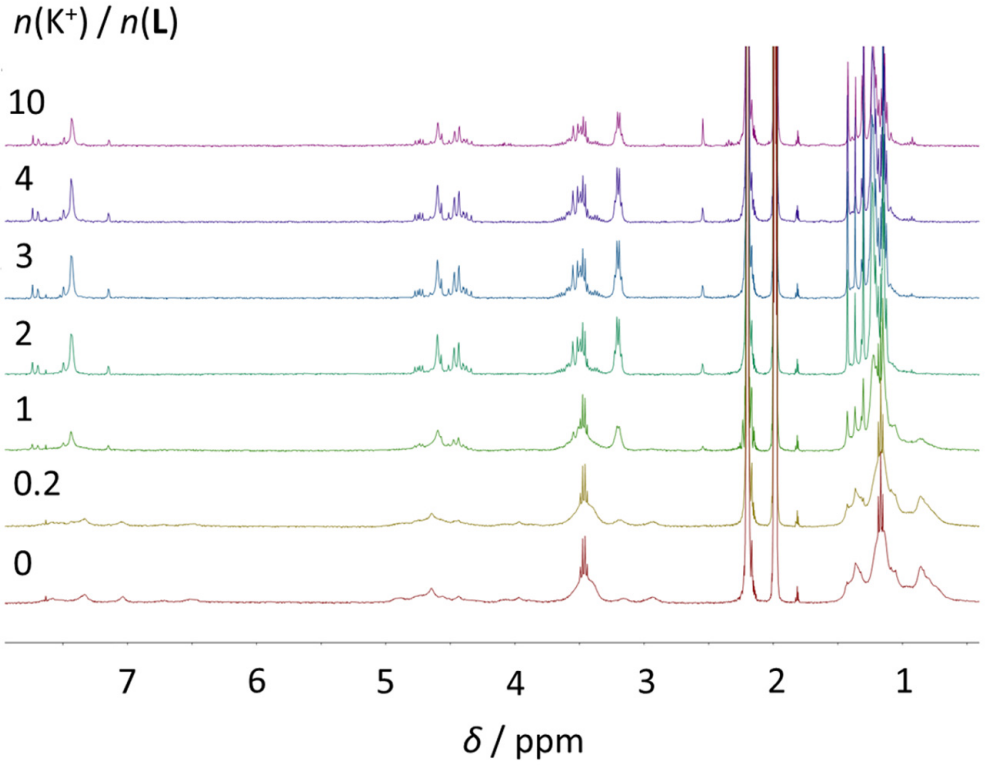


Figure 6. ^{1}H NMR titration of **L** ($c = 1.01 \times 10^{-3}$ mol dm^{-3}) with $KClO_4$ ($c = 1.01 \times 10^{-2}$ mol dm^{-3}) in CD_3CN; $\vartheta = (25.0 \pm 0.1)$ °C.

For all alkaline earth metal cations, complexation resulted in decreased fluorescence intensity and a shift in the emission maximum toward shorter wavelengths (Figures 7 and S29–S31), accompanied by the appearance of an isosbestic point (Figures 7, S30 and S31). The linear dependence of RIF on the $n(M^{2+})/n(\mathbf{L})$ ratio up to ≈1, followed by negligible further changes in intensity, suggests the formation of highly stable complexes of 1:1 stoichiometry. This was confirmed by UV absorption titrations (the only exception being Mg^{2+}, see below), in which the same trends in the dependence of absorbance on the $n(M^{2+})/n(\mathbf{L})$ ratio were observed (Figures 8, S33 and S34), as well as by the corresponding ITC experiments (Figures S35–S38). Consistently, in contrast to univalent cations, mass spectra of solutions containing **L** and divalent metal salts showed only signals corresponding to 1:1 complexes ($[\mathbf{L} + M]^{2+}$) (Table S2, Figures S39–S42). Furthermore, in all related ^{1}H NMR titrations, spectral changes occurred up to 1:1 molar ratio, with practically no further alterations beyond this point (Figures 9, S43 and S44; see also the corresponding distribution diagrams shown in Figures S45–S47). The absence of 2:1 complexes with the second-group metal ions can be attributed primarily to the strongly unfavorable electrostatic repulsion between the divalent cations which would exist within such species. However, it is worth noting that the changes in the UV absorption spectra observed during titration of **L** with Mg^{2+} suggested formation of both 1:1 and 2:1 complexes (Figure S32). The stability constant of the former appeared to be too high to be reliably determined, as indicated by the nearly linear dependence of the absorbance on $n(Mg^{2+})/n(\mathbf{L})$ ratio up to ≈1. Moreover, equally satisfactory fits, yielding virtually identical calculated spectra and residual standard deviations, were obtained for any assumed value of the 1:1 complex stability constant in the range of $7 \leq \log K \leq 10$,

whereas the fitted value of the 2:1 stability constant remained essentially unchanged. This is a consequence of the fact that the 1:1 complex is formed practically stoichiometrically for any log $K(\mathrm{MgL}^{2+}) \geq 7$, so that only the lower limit of 10^7 for this constant can be estimated. That allowed us to separately process the titration data corresponding to cation-to-ligand molar ratios greater than 1 by considering only the equilibrium between MgL^{2+} and $\mathrm{Mg_2L}^{4+}$. The initial concentration of MgL^{2+} was reasonably assumed to be equal to the analytical concentration of the ligand, thereby simplifying the analysis to a 1:1 binding model. Very good agreement between the experimental and calculated data was obtained (Figure S32), yielding a value of log $K(\mathrm{Mg_2L}^{4+}) = 3.94 \pm 0.05$. The fact that fluorimetry (Figure S29) and mass spectrometry (Figure S39) revealed only complex of 1:1 stoichiometry is most likely a consequence of the much lower ligand concentrations used in these experiments. Based on the stability constant of $\mathrm{Mg_2L}^{4+}$, the abundance of this species at such concentrations is expected to be too low for its reliable detection.

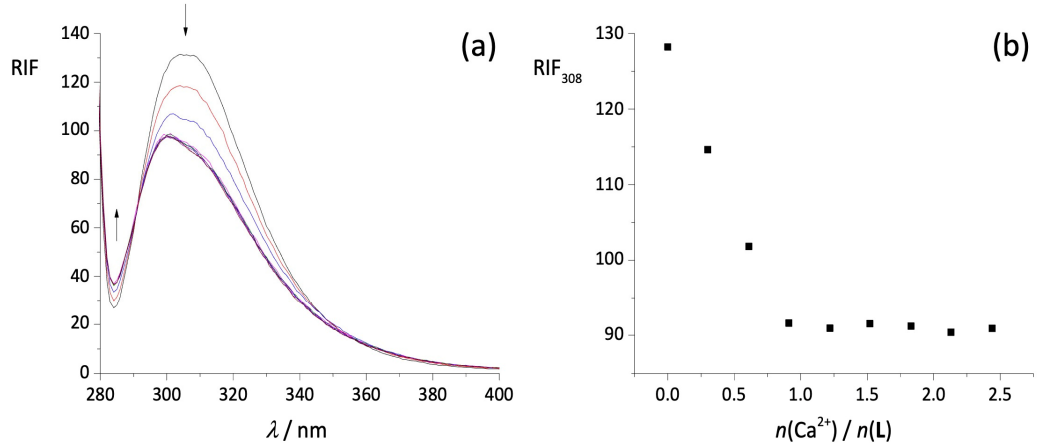


Figure 7. (**a**) Fluorimetric titration of **L** ($c = 1.26 \times 10^{-5}$ mol dm^{-3}) with $Ca(ClO_4)_2$ ($c = 9.58 \times 10^{-4}$ mol dm^{-3}) in MeCN; $\vartheta = (25.0 \pm 0.1)$ °C; V_0(**L**) = 2.5 cm^3; λ_{exc} = 272 nm; excitation slit 5 nm, emission slit 10 nm. Spectra are corrected for dilution. (**b**) Dependence of the relative intensity of **L** fluorescence at 308 nm on the cation-to-ligand molar ratio.

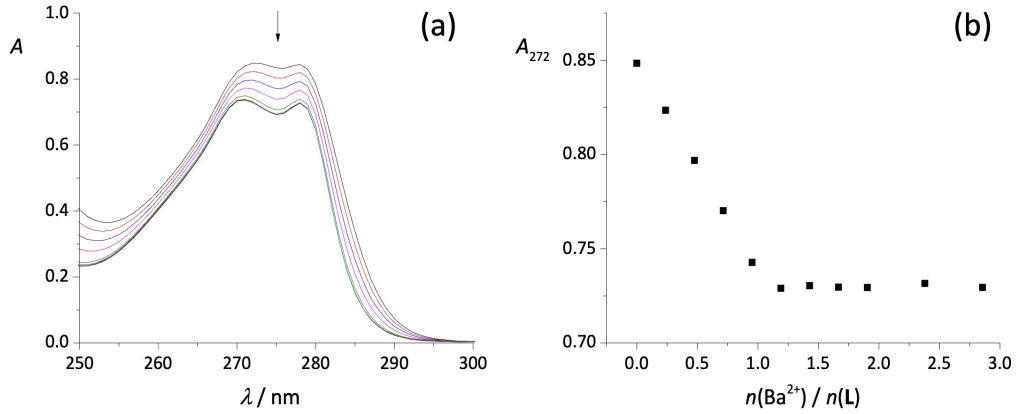


Figure 8. (**a**) Spectrophotometric titration of **L** ($c = 1.99 \times 10^{-4}$ mol dm^{-3}) with $Ba(trf)_2$ ($c = 2.08 \times 10^{-3}$ mol dm^{-3}) in MeCN; $\vartheta = (25.0 \pm 0.1)$ °C; V_0(**L**) = 2.2 cm^3; l = 1 cm. Spectra are corrected for dilution. (**b**) Dependence of the absorbance of **L** at 272 nm on the cation-to-ligand molar ratio.

The above results regarding the stability and composition of the complexes are consistent with previous literature findings [49,52,56,79,80]. However, the affinity of **L** for the alkaline earth metal ions is so high that essentially quantitative complexation occurred over the accessible concentration range, preventing determination of the corresponding ML^{2+}

stability constants even by direct spectrofluorimetric titrations. Nevertheless, the observed linear fluorescence response may be of interest from an analytical point of view.

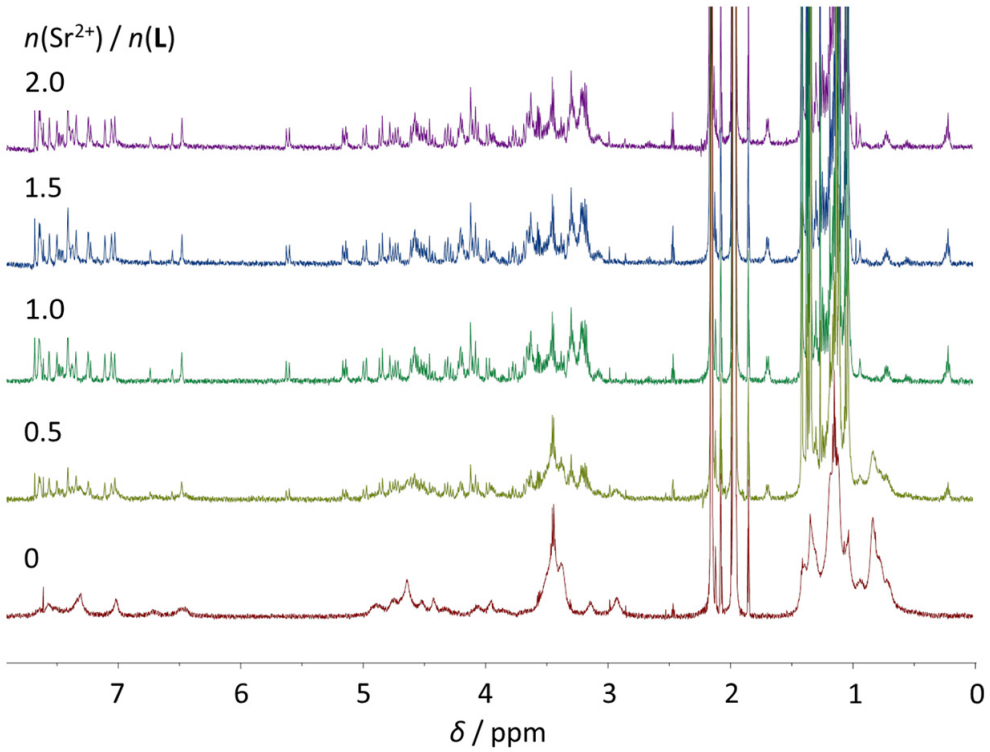


Figure 9. ^{1}H NMR titration of **L** ($c = 2.57 \times 10^{-4}$ mol dm^{-3}) with $Sr(ClO_4)_2$ ($c = 1.03 \times 10^{-2}$ mol dm^{-3}) in CD_3CN; $\vartheta = (25.0 \pm 0.1)$ °C.

3.3. Origins of Fluorescence Changes upon Complexation

The changes in fluorescence intensity observed upon cation binding (the corresponding fluorescence quantum yields are presented in Table S3), as well as the blue shifts in the emission spectra, can be rationalized in terms of several possible complementary effects. For most cations, the increase or decrease in fluorescence is directly related to the change in absorbance at the excitation wavelength. If the molar absorption coefficient of the complex exceeds that of the free ligand, as is the case for K^+ and Rb^+ (Figures S10 and S11), the fluorescence intensity increases in the course of the corresponding titration (Figures 4 and S4–S6), whereas the opposite trend holds for Li^+ and Cs^+ (Figures S3, S7, S8 and S12). This can be readily explained by the larger or smaller fraction of absorbed photons, resulting in different populations of excited species. However, this excitation-emission correlation does not hold for sodium ion complexation (compare Figures 3 and S9). Furthermore, titration of **L** with K^+ using an excitation wavelength corresponding to the isosbestic point observed during the UV absorption titration again resulted in fluorescence enhancement, with a very similar dependence of the RIF on the cation concentration (Figure S48). These two observations indicate that the fluorescence changes cannot be attributed solely to differences in absorbance at the excitation wavelength and that additional factors also contribute. First, complexation induces conformational rigidification of the receptor framework, which suppresses non-radiative relaxation pathways and consequently enhances fluorescence emission. The impact of non-radiative deactivation associated with internal molecular motions is consistent with the observed decrease in fluorescence intensity along the series: the monomeric compound constituting the tertiary-amide calixarene derivatives ($\Phi_f = 5.9\%$) > the corresponding calix[4]arene derivative ($\Phi_f = 1.3\%$) > the more flexible calix[6]arene derivative **L** ($\Phi_f = 0.9\%$). This interpretation is further supported by the signif-

icantly higher fluorescence of the parent lower-rim-unsubstituted calix[6]arene (Φ_f = 10%) compared with **L**. In the parent calixarene, conformational motions are restricted by the presence of intramolecular phenolic OH···O hydrogen bonds, whereas **L** contains flexible $–OCH_2CON(Et)_2$ substituents which introduce additional vibrational modes and conformational degrees of freedom. These additional motions provide efficient non-radiative decay pathways, thereby reducing the fluorescence intensity. Second, the suppression of photoinduced electron transfer (PET) from donor ether oxygen atoms to the excited aromatic system upon cation binding should also be considered. In the free ligand, PET provides an efficient non-radiative deactivation pathway and is likely one of the factors responsible for the relatively low intrinsic fluorescence of the calixarene derivative **L**. Upon complexation, electrostatic interactions between the metal ion and the donor oxygen atoms stabilize their lone-pair orbitals and thus decrease their electron-donating ability and make PET thermodynamically less favorable. As a consequence, PET-induced fluorescence quenching is suppressed, resulting in enhanced emission. The comparison of **L** with the unsubstituted parent calix[6]arene is also relevant in this context. As already mentioned, in the latter compound the phenolic oxygen atoms participate in an intramolecular hydrogen-bonding network, which lowers the energy of their lone-pair electrons, thereby reducing their donor ability and disfavoring PET. This effect may provide an additional contribution to the higher fluorescence of the parent calixarene relative to the substituted derivative **L**.

Although the effects discussed above provide plausible explanations for the differences in fluorescence intensity between the free and complexed **L**, they do not directly account for the observed changes in emission wavelengths. Despite being relatively small (approximately 540 to 760 cm^{-1}), the systematic blue shift accompanying complexation, together with its slight dependence on the bound cation, suggests an additional contribution arising from changes in the electronic structure following the excitation. In the absence of further information, this could tentatively be interpreted in terms of a possible intramolecular charge-transfer (ICT) character of the excited state. As discussed above, the ground state of the complex is stabilized by the electrostatic interactions between the cation and the donor oxygen atoms. If excitation involves partial charge transfer from these atoms toward the aromatic system, the electron density at the coordinating oxygen atoms decreases. Consequently, the cation stabilizes the emissive excited state less effectively than the ground state, increasing the energy gap between them and giving rise to the observed blue shift in the emission maximum.

Even though all the factors proposed for alkali metal ion complexation should also operate for alkaline earth metal cations, the uniform decrease in fluorescence observed for the latter (Figures 7 and S29–S31) is presumably by large part a consequence of the significantly more pronounced hypochromic effect of divalent cation binding on the absorption spectrum of **L** (Figures 8 and S32–S34). In other words, for all second-group metal ions, the lower extent of excitation of complex species relative to the free ligand overcomes the other effects and results in decreased fluorescence intensity. In addition, despite the larger charge density of divalent cations, the weakening of their ability to suppress PET can be rationalized by taking into account two structural features revealed by the corresponding molecular dynamics simulations (see next section). First, alkaline earth metal ions prefer coordination with the carbonyl oxygen atoms in the binding site of the ligand, thereby reducing their electrostatic influence on the ether oxygen atoms involved in the PET process. Second, unlike the alkali metal cations, the divalent ones are coordinated not only by the acetonitrile molecule included within the calixarene *basket* but also with another solvent molecule approaching from the lower-rim side of the ligand. This additional coordination is also expected to lower the ability of inhibiting PET by the complexed cation.

The molecular dynamics simulations revealed distinct complex geometries which depend on both the size and charge of the metal ion and are likely to affect the fluorescence response through several mechanisms. However, it should be noted that the MD simulations describe the ground-state coordination geometry and solvation of the complexes and cannot by themselves confirm the above interpretation, which requires excited-state calculations.

3.4. Results of MD Simulations

All examined complexes remained stable over the entire course of the molecular dynamics simulations, and the coordination environments of the metal ions were generally well preserved. The alkali metal cations are coordinated on average by approximately two ether and three carbonyl oxygen atoms, with very similar coordination patterns in both the 1:1 and 2:1 complexes (Figure 10, Tables S4 and S5). The only notable exception is lithium, for which the average number of coordinated ether oxygen atoms increases from on average 1.3 in the 1:1 to 2.0 in the 2:1 complex. The alkaline earth metal cations exhibit a stronger preference for coordination by carbonyl oxygen atoms (Figure 11, Table S6). Magnesium and calcium ions are coordinated predominantly by four carbonyl oxygen atoms, whereas strontium and barium interact with five. In addition, all alkaline earth cations except magnesium interact with approximately two ether oxygen atoms. Magnesium cation appears not to be coordinated by the latter atoms, indicating a hexacoordinate environment consisting of four equatorial carbonyl oxygen atoms and two axial acetonitrile molecules (Figure 11). Further information on the coordination geometries of the most populated binding modes is provided in Tables S4–S6.

Besides direct coordination by the ligand oxygen atoms, the simulations revealed several characteristic features of solvent participation in the coordination sphere of the metal ions. As shown in Figures 10 and 11, in all 1:1 complexes, a single acetonitrile molecule is included in the calixarene cavity and coordinates the metal cation through its nitrile group. In all cases except the $Cs\mathbf{L}^+$ complex, the same acetonitrile molecule remains bound throughout the simulation, indicating a stable host-solvent interaction (Figures 10 and S49). For the 1:1 complexes of K^+, Rb^+, and Cs^+, transient coordination of the metal cation with acetonitrile molecule from the lower rim of the calixarene was also observed. These interactions are short-lived and involve the continuous exchange of solvent molecules. In contrast, the alkaline earth metal complexes exhibit considerably more persistent solvent coordination from the lower rim (Figures 11 and S51). A single acetonitrile molecule typically remains coordinated for extended periods, with only occasional exchange by another solvent molecule. A second acetonitrile molecule is also sporadically included within the calixarene cavity, although such events are generally short-lived.

The solvent binding pattern becomes more complex in the 2:1 complexes (Figures 10 and S50). In the $Li_2\mathbf{L}^{2+}$, a single acetonitrile molecule is included in the cavity and only occasionally coordinates one of the lithium ions through its nitrile nitrogen atom, while it is predominantly oriented with its methyl group facing the cation. In the $Na_2\mathbf{L}^{2+}$, the included acetonitrile molecule alternately coordinates one or the other sodium ion. Whenever one cation is coordinated through the cavity, the second cation is occasionally coordinated by acetonitrile molecule approaching from the lower rim of the complex. In the $K_2\mathbf{L}^{2+}$, $Rb_2\mathbf{L}^{2+}$, and $Cs_2\mathbf{L}^{2+}$, two acetonitrile molecules are accommodated within the cavity. One of them is simultaneously bound to both metal cations, whereas the second coordinates only one of them, resulting in one cation being coordinated by two solvent molecules and the other by only one. The latter cation is also occasionally coordinated by an additional acetonitrile molecule from the lower rim of the complex. This is more pronounced for the rubidium and cesium complexes than for the potassium analog. In the

complex species comprising two relatively large cations ($K_2\mathbf{L}^{2+}$, $Rb_2\mathbf{L}^{2+}$, and $Cs_2\mathbf{L}^{2+}$), a certain degree of asymmetry in the coordination environments, which increases with the cation size, was observed (Figures 10 and S50). This asymmetry arises from the inability of two large cations to be symmetrically accommodated at the same level, i.e., to occupy equivalent positions, within the **L** binding site. It is particularly evident in the case of $Cs_2\mathbf{L}^{2+}$, in which one of the Cs^+ ions adopts an essentially *exo*-bound position outside the calixarene cavity. Such an arrangement is expected to considerably weaken the 2:1 complex stability, in accordance with the experimental findings.

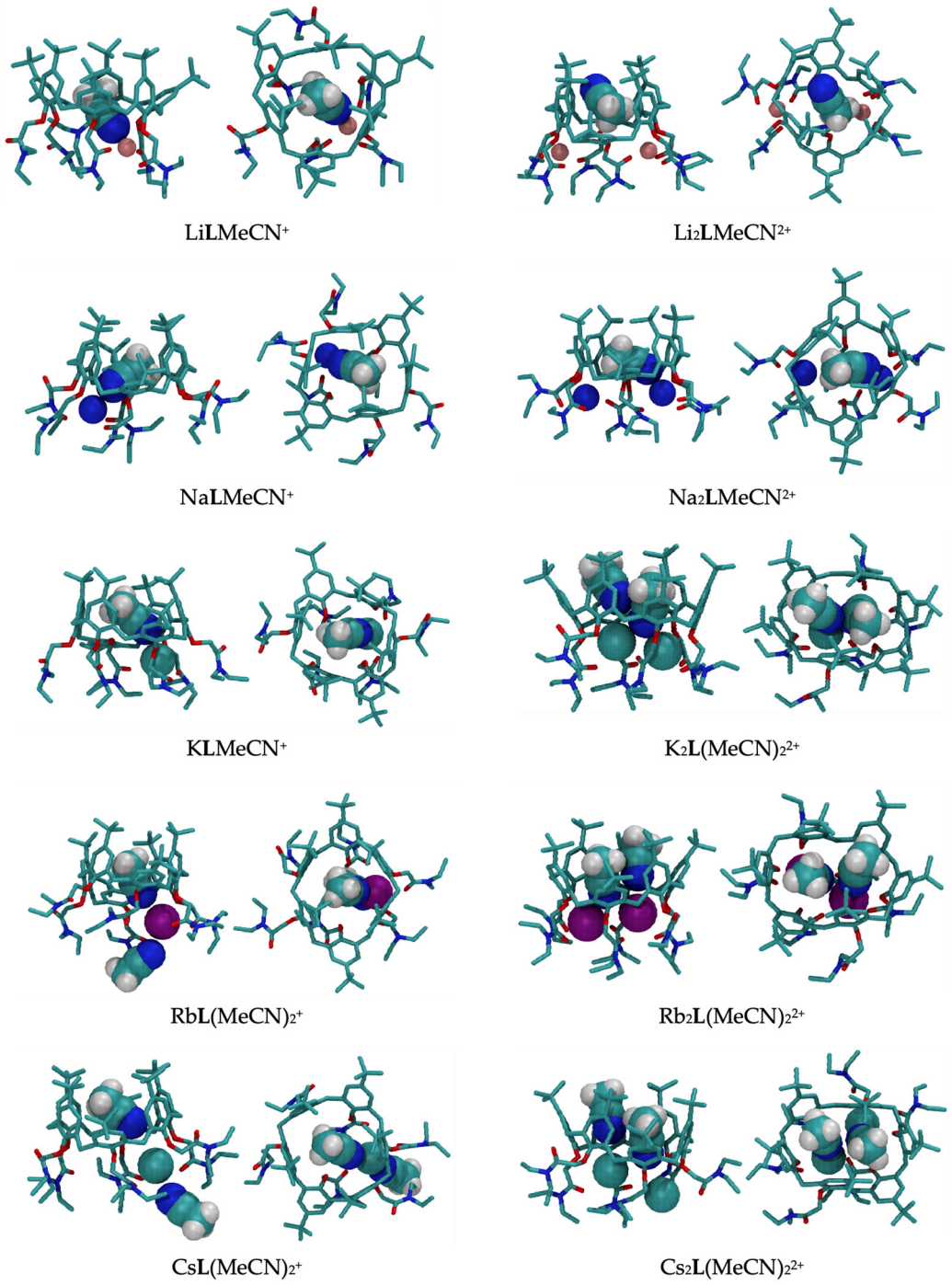


Figure 10. Representative structures of $M\mathbf{L}^+$ and $M_2\mathbf{L}^{2+}$ complexes in acetonitrile obtained by MD simulations at 25 °C. Hydrogen atoms of **L** are omitted for clarity.

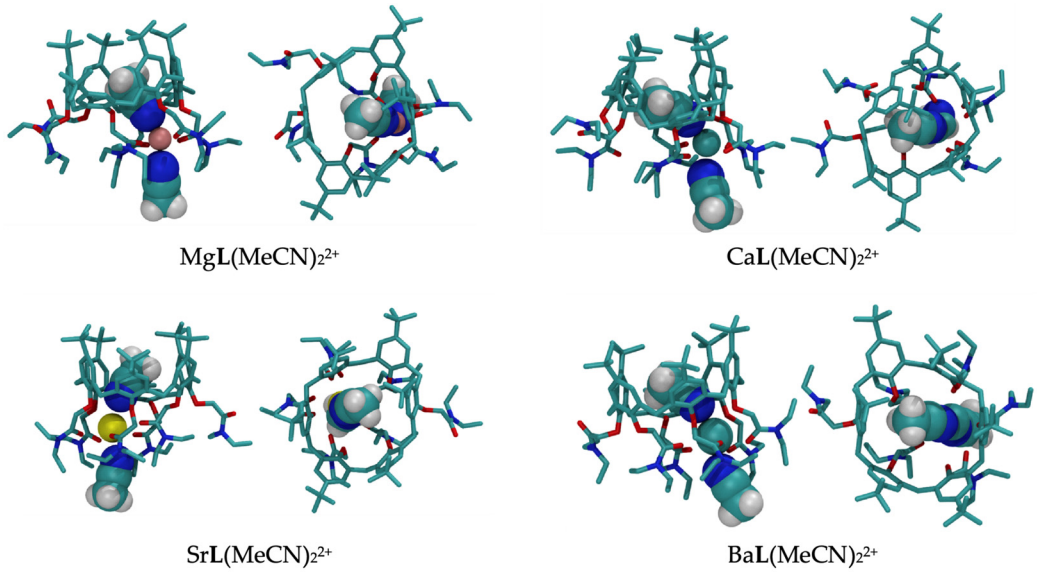


Figure 11. Representative structures of M**L**$^{2+}$ complexes in acetonitrile obtained by MD simulations at 25 °C. Hydrogen atoms of **L** are omitted for clarity.

4. Conclusions

In this work, it was demonstrated that monitoring changes in the intrinsic fluorescence of calix[6]arene amide derivative **L** provides a valuable and sensitive tool for the quantitative characterization of its cation-complexation reactions, offering clear advantages over other commonly used methods, despite the belief that calixarenes lacking appended fluorophore(s) cannot serve as luminescent probes [4]. For that purpose, spectrofluorimetric titrations of **L** with a series of alkali and alkaline earth metal cations in acetonitrile solution were carried out. Although the ligand exhibited only moderate fluorescence, its emission was substantially affected by cation binding. Analyses of the titration data enabled the determination of the complex stability constants, which were in very good agreement with those obtained by comparative UV absorption and ITC titrations. Univalent cations were found to form both 1:1 and 2:1 (cation:ligand) complexes, whereas divalent metal ions formed exclusively 1:1 species, as the electrostatic repulsion between the highly charged cations prevented the formation of higher-order complexes. It should be noted that large stability constants (log $K > 6$) could only be determined by fluorimetry owing to its considerably higher sensitivity, which also allowed the working concentrations of **L** to be significantly lowered, in some instances even by nearly two orders of magnitude compared to other techniques. The stoichiometries of the complexes were supported by mass spectrometry and ^{1}H NMR titrations. The latter also clearly indicated the expected rigidification of the ligand upon cation binding. Molecular dynamics simulations further provided insight into the structures of the complexes and the cation coordination sites.

Interestingly, the complexation-induced fluorescence response was found to be quite cation-specific. For the alkali metal ions, substantial fluorescence enhancement (K^+ and Rb^+), quenching (Li^+ and Cs^+), or both (Na^+, depending on its concentration) were observed, whereas binding of all second-group metal ions resulted in fluorescence quenching. The complementary factors that presumably govern the changes in fluorescence intensity and the accompanying spectral blue shift upon cation complexation, including conformational rigidification, the population of the excited state, photoinduced electron transfer, and intramolecular charge transfer, were discussed. However, the arguments presented for the effects of the latter two processes are based on qualitative reasoning, which is consistent

with the available data but requires support from quantum-chemical TD-DFT calculations. Such an approach is therefore planned as a continuation of the work on this subject.

Overall, this work highlights the potential of monitoring intrinsic fluorescence for sensitive, quantitative characterization of cation-complexation reactions of calixarenes at substantially reduced receptor concentrations compared to other frequently used methods. Furthermore, this approach enables the determination of large stability constants by direct spectrofluorimetric titrations, without requiring time- and material-consuming competitive titrations. The findings of this and our previous work [10] suggest that this methodology may prove applicable not only to calixarenes but also to other intrinsically fluorescent macrocycles, thereby broadening the scope of fluorescence-based studies of supramolecular complexation.

Supplementary Materials: The following supporting information can be downloaded at https://www.mdpi.com/article/10.3390/analytica7040072/s1, Figures S1 and S2, Emission properties of **L**; Figures S3–S7, Fluorimetric titrations with alkali metal cations; Figures S8–S12, Spectrophotometric titrations with alkali metal cations; Figures S13–S16, Microcalorimetric titrations with alkali metal cations; Table S1, Figures S17–S22, Mass spectra of **L** and its complexes with alkali metal cations; Figures S23–S27, ^{1}H NMR titrations with alkali metal cations and the corresponding distribution diagrams; Figure S28, Selectivity of **L** towards alkali metal cations; Figures S29–S31, Fluorimetric titrations with alkaline earth metal cations; Figures S32–S34, Spectrophotometric titrations with alkaline earth metal cations; Figures S35–S38, Microcalorimetric titrations with alkaline earth metal cations; Table S2, Figures S39–S42, Mass spectra of **L** and its complexes with alkaline earth metal cations; Figures S43–S47, ^{1}H NMR titrations with alkaline earth metal cations and the corresponding distribution diagrams; Description of fluorescence quantum yields determination; Table S3, Quantum yields of selected complexes, calixarenes, and the monomer; Figure S48, Fluorimetric titration with $KClO_4$ with excitation wavelength set to that corresponding to an isosbestic point; Figures S49–S50, Index numbers of MeCN molecules that occupy the hydrophobic cavity of alkali metal complexes and those that coordinate the cation from either the cavity or the lower-rim side of the ligand during MD simulations in MeCN; Tables S4 and S5, The number of ether and carbonyl groups which coordinate alkali metal cations in complexes and the dominant binding modes of each cation obtained by MD simulations in MeCN, Figure S51, Index numbers of MeCN molecules that occupy the hydrophobic cavity of alkaline earth metal complexes and those that coordinate the cation from either the cavity or the lower-rim side of the ligand during MD simulations in MeCN; Table S6, The number of ether and carbonyl groups which coordinate alkaline earth metal cations in complexes and the dominant binding modes of each cation obtained by MD simulations in MeCN.

Author Contributions: Conceptualization, A.U., I.P. and V.T.; methodology, A.U., F.S., L.K., K.L., N.C., G.H. and V.T.; software, G.H.; validation, A.U., F.S., L.K., G.H. and V.T.; formal analysis, A.U., F.S., K.K.G., L.K., K.L. and V.T.; investigation, A.U., F.S., K.K.G., L.K., K.L., N.C. and G.H.; resources, A.U., K.L., N.C., G.H., I.P. and V.T.; data curation, A.U., F.S., K.K.G., L.K., K.L., G.H. and V.T.; writing—original draft preparation, A.U. and V.T.; writing—review and editing, A.U., F.S., L.K., G.H., I.P. and V.T.; visualization, A.U., F.S., L.K., G.H. and V.T.; supervision, A.U., K.L., N.C. and V.T.; project administration, V.T.; funding acquisition, N.C., G.H., I.P. and V.T. All authors have read and agreed to the published version of the manuscript.

Funding: This research was funded by the Croatian Science Foundation (projects CalixCORE (IP-2024-05-3012), MacroSol (IP-2019-04-9560), POC-Sens-Bioact (IP-2022-10-9829), CPepFunxIon (IP-2025-02-8238) and MicroSynTotal (IP-2024-05-5352)), European Union—NextGenerationEU through the National Recovery and Resilience Plan 2021−2026. via Institutional grants of the University of Zagreb Faculty of Science (NextGenChem and CryoLab) and project ToSiAn (NPOO.C3.2.R2-I1.06.0043), and the European Regional Development Fund (infrastructural project CIuK (KK.01.1.1.02.0016)).

Data Availability Statement: The original contributions presented in this study are included in the article/Supplementary Materials. Further inquiries can be directed to the corresponding authors.

Conflicts of Interest: The authors declare no conflicts of interest.

Abbreviations

The following abbreviations are used in this manuscript:

RIF	Relative intensity of fluorescence
ITC	Isothermal titration calorimetry
NMR	Nuclear magnetic resonance
MS	Mass spectrometry
MD	Molecular dynamics (simulations)
MeCN	Acetonitrile
ICT	Intramolecular charge transfer
PET	Photoinduced electron transfer
UV-Vis	Ultraviolet-visible
Q-TOF	Quadrupole time-of-flight
HPLC	High-performance liquid chromatography
exc	Excitation
em	Emission
FLUO	Fluorimetry
SE	Standard error of the mean
Et	Ethyl
trf^-	triflate (trifluoromethanesulfonate)

References

1. Asfari, Z.; Böhmer, V.; Harrowfield, J.; Vicens, J. (Eds.) *Calixarenes 2001*; Kluwer Academic Publishers: Dordrecht, The Netherlands, 2001.
2. Gutsche, C.D. *Calixarenes: An Introduction*, 2nd ed.; Monographs in Supramolecular Chemistry; RSC Publishing: Cambridge, UK, 2008.
3. Baldini, L.; Sansone, F.; Casnati, A.; Ungaro, R. Calixarenes in Molecular Recognition. In *Supramolecular Chemistry*; Gale, P.A., Steed, J.W., Eds.; Wiley: Hoboken, NJ, USA, 2012.
4. Neri, P.; Sessler, J.L.; Wang, M.-X. (Eds.) *Calixarenes and Beyond*; Springer International Publishing: Cham, Switzerland, 2016.
5. Macreadie, L.K.; Gilchrist, A.M.; McNaughton, D.A.; Ryder, W.G.; Fares, M.; Gale, P.A. Progress in Anion Receptor Chemistry. *Chem* **2022**, *8*, 46–118. [CrossRef]
6. El Nashar, R.M.; Wagdy, H.A.A.; Aboul-Enein, H.Y. Applications of Calixarenes as Potential Ionophores for Electrochemical Sensors. *Curr. Anal. Chem.* **2009**, *5*, 249–270. [CrossRef]
7. Evtugyn, G.A.; Stoikova, E.E.; Shamagsumova, R.V. Molecular Receptors and Electrochemical Sensors Based on Functionalized Calixarenes. *Russ. Chem. Rev.* **2010**, *79*, 1071–1097. [CrossRef]
8. Kumar, R.; Sharma, A.; Singh, H.; Suating, P.; Kim, H.S.; Sunwoo, K.; Shim, I.; Gibb, B.C.; Kim, J.S. Revisiting Fluorescent Calixarenes: From Molecular Sensors to Smart Materials. *Chem. Rev.* **2019**, *119*, 9657–9721. [CrossRef] [PubMed]
9. Marcos, P.M.; Berberan-Santos, M.N. Recent Advances in Calixarene-Based Fluorescent Sensors for Biological Applications. *Sensors* **2024**, *24*, 7181. [CrossRef] [PubMed]
10. Usenik, A.; Nikšić-Franjić, I.; Belovari, M.; Jurković, M.; Klemen, L.; Cindro, N.; Došlić, N.; Piantanida, I.; Tomišić, V. Intrinsic Fluorescence of Calixarenes: The Origin and Applications. *Anal. Chim. Acta* **2025**, *1377*, 344648. [CrossRef] [PubMed]
11. Martins, J.N.; Pessêgo, M.; Garcia-Rio, L.; Lima, J.C.; Basílio, N. Induced-Fit Recognition by a Calixarene–Pyrene Conjugate for Single- and Dual-Wavelength Fluorescence Sensing in Water. *Chem.—Eur. J.* **2026**, *32*, e03407. [CrossRef] [PubMed]
12. Ren, H.; Wang, H.; Wen, W.; Li, S.; Li, N.; Huo, F.; Yin, C. A Summary of Calixarene-Based Fluorescent Sensors Developed during the Past Five Years. *Chem. Commun.* **2023**, *59*, 13790–13799. [CrossRef] [PubMed]
13. Ludwig, R.; Dzung, N. Calixarene-Based Molecules for Cation Recognition. *Sensors* **2002**, *2*, 397–416. [CrossRef]
14. Arnaud-Neu, F.; Barrett, G.; Fanni, S.; Marrs, D.; McGregor, W.; McKervey, M.A.; Schwing-Weill, M.-J.; Vetrogon, V.; Wechsler, S. Extraction and Solution Thermodynamics of Complexation of Alkali and Alkaline-Earth Cations by Calix[4]Arene Amides. *J. Chem. Soc. Perkin Trans. 2* **1995**, *24*, 453–461. [CrossRef]
15. Sviben, I.; Galić, N.; Tomišić, V.; Frkanec, L. Extraction and Complexation of Alkali and Alkaline Earth Metal Cations by Lower-Rim Calix[4]Arene Diethylene Glycol Amide Derivatives. *New J. Chem.* **2015**, *39*, 6099–6107. [CrossRef]

16. Aparicio-Aragon, W.B.; Ramos, T.D.; Danil de Namor, A.F. Effect of the Number of Donor Atoms in Calix[4]Arene Derivatives for Selective Complexation and Extraction of Mercury(II) Cations, Thermodynamics and Extraction Studies. *Adv. Chem. Eng. Sci.* **2021**, *11*, 165–179. [CrossRef]
17. Oshima, T.; Ishibashi, T.; Ohto, K. Solubilities and Metal Extraction Behaviors for Calix[4]Arene Acetic-Acid Derivatives in Various Organic Solvents. *J. Incl. Phenom. Macrocycl. Chem.* **2023**, *103*, 71–79. [CrossRef]
18. Creaven, B.S.; Donlon, D.F.; McGinley, J. Coordination Chemistry of Calix[4]Arene Derivatives with Lower Rim Functionalisation and Their Applications. *Coord. Chem. Rev.* **2009**, *253*, 893–962. [CrossRef]
19. Wei, A. Calixarene-Encapsulated Nanoparticles: Self-Assembly into Functional Nanomaterials. *Chem. Commun.* **2006**, *42*, 1581–1591. [CrossRef] [PubMed]
20. Zhang, F.; Sun, Y.; Tian, D.; Shin, W.S.; Kim, J.S.; Li, H. Selective Molecular Recognition on Calixarene-Functionalized 3D Surfaces. *Chem. Commun.* **2016**, *52*, 12685–12693. [CrossRef] [PubMed]
21. Rodik, R.; Cherenok, S.; Kalchenko, O.; Yesypenko, O.; Lipkowski, J.; Kalchenko, V. Functional Calixarenes for Material and Life Science. *Curr. Org. Chem.* **2018**, *22*, 2200–2222. [CrossRef]
22. Tian, J.; Shi, B.; Lin, Q. Strategies for Enhancing Macrocyclic Host–Guest Properties. *Acc. Chem. Res.* **2026**, *59*, 1905–1917. [CrossRef] [PubMed]
23. Araki, K.; Yanagi, A.; Shinkai, S. Optimization of Phase-Transfer Catalysts Designed from Calix[4]Arene. *Tetrahedron* **1993**, *49*, 6763–6772. [CrossRef]
24. Sachdeva, G.; Vaya, D.; Srivastava, C.M.; Kumar, A.; Rawat, V.; Singh, M.; Verma, M.; Rawat, P.; Rao, G.K. Calix[*n*]Arenes and Its Derivatives as Organocatalysts. *Coord. Chem. Rev.* **2022**, *472*, 214791. [CrossRef]
25. Agrawal, Y.K.; Bhatt, H. Calixarenes and Their Biomimetic Applications. *Bioinorg. Chem. Appl.* **2004**, *2*, 237–274. [CrossRef] [PubMed]
26. Sansone, F.; Baldini, L.; Casnati, A.; Ungaro, R. Calixarenes: From Biomimetic Receptors to Multivalent Ligands for Biomolecular Recognition. *New J. Chem.* **2010**, *34*, 2715. [CrossRef]
27. Schühle, D.T.; Peters, J.A.; Schatz, J. Metal Binding Calixarenes with Potential Biomimetic and Biomedical Applications. *Coord. Chem. Rev.* **2011**, *255*, 2727–2745. [CrossRef]
28. Wang, J.; Ding, X.; Guo, X. Assembly Behaviors of Calixarene-Based Amphiphile and Supra-Amphiphile and the Applications in Drug Delivery and Protein Recognition. *Adv. Colloid Interface Sci.* **2019**, *269*, 187–202. [CrossRef] [PubMed]
29. Pan, Y.; Hu, X.; Guo, D. Biomedical Applications of Calixarenes: State of the Art and Perspectives. *Angew. Chem. Int. Ed.* **2021**, *60*, 2768–2794. [CrossRef] [PubMed]
30. Aoun, P.; Nyssen, N.; Richard, S.; Zhurkin, F.; Jabin, I.; Colasson, B.; Reinaud, O. Selective Metal-ion Complexation of a Biomimetic Calix[6]Arene Funnel Cavity Functionalized with Phenol or Quinone. *Chem.—Eur. J.* **2023**, *29*, e202202934. [CrossRef] [PubMed]
31. Martins, J.N.; Raimundo, B.; Rioboo, A.; Folgar-Cameán, Y.; Montenegro, J.; Basílio, N. Photoswitchable Calixarene Activators for Controlled Peptide Transport across Lipid Membranes. *J. Am. Chem. Soc.* **2023**, *145*, 13126–13133. [CrossRef] [PubMed]
32. Wu, X.; Yao, S.; Huang, Q.; Ying, A.; Li, Q.; Cao, X.; Wang, C.; Xiao, J.; Feng, N.; Zhang, Z.; et al. Antibody–Calixarene Drug Conjugate: A General Drug Delivery Platform for Tumor-Targeted Therapy. *ACS Appl. Mater. Interfaces* **2024**, *16*, 41939–41948. [CrossRef] [PubMed]
33. Muley, S.; Dhila, H.; Gote, M. Calixarene-Guest Complexes: The Next Innovation in Delivery of Drugs and Biologics. *Adv. Ther.* **2024**, *7*, 2400207. [CrossRef]
34. Pandey, P.; Singh, R.; Mishra, M.K.; Srivastava, R. Calixarene in Chemotherapy Drug Delivery: Its Role and Strategies. *Curr. Cancer Ther. Rev.* **2025**, *21*, 245–253. [CrossRef]
35. Nimse, S.B.; Kim, T. Biological Applications of Functionalized Calixarenes. *Chem. Soc. Rev.* **2013**, *42*, 366–386. [CrossRef] [PubMed]
36. Dondoni, A.; Marra, A. Calixarene and Calixresorcarene Glycosides: Their Synthesis and Biological Applications. *Chem. Rev.* **2010**, *110*, 4949–4977. [CrossRef] [PubMed]
37. Krošl, I.; Otković, E.; Nikšić-Franjić, I.; Colasson, B.; Reinaud, O.; Višnjevac, A.; Piantanida, I. Impact of Positive Charge and Ring-Size on the Interactions of Calixarenes with DNA, RNA and Nucleotides. *New J. Chem.* **2022**, *46*, 6860–6869. [CrossRef]
38. Danil de Namor, A.F.; Gil, E.; Tanco, M.A.L.; Tanaka, D.A.P.; Salazar, L.E.P.; Schulz, R.A.; Wang, J. Thermodynamics of Calix[4]Arene Esters. 1. Complexation of Alkyl *p-Tert*-Butylcalix[4]Arenetetraethanoates and Alkali-Metal Cations in Acetonitrile and in Benzonitrile. *J. Phys. Chem.* **1995**, *99*, 16776–16780. [CrossRef]
39. Danil de Namor, A.F.; Cleverley, R.M.; Zapata-Ormachea, M.L. Thermodynamics of Calixarene Chemistry. *Chem. Rev.* **1998**, *98*, 2495–2526. [CrossRef] [PubMed]
40. Danil de Namor, A.F.; Kowalska, D.; Castellano, E.E.; Piro, O.E.; Sueros Velarde, F.J.; Villanueva Salas, J. Lower Rim Calix[4]Arene Ketone Derivatives and Their Interaction with Alkali Metal Cations. Structural and Thermodynamic (Solution and Complexation) Characterisation of the Tetraphenyl Ketone Derivative and Its Sodium Complex. *Phys. Chem. Chem. Phys.* **2001**, *3*, 4010–4021. [CrossRef]

41. Danil de Namor, A.F.; Chahine, S.; Castellano, E.E.; Piro, O.E. Solvent Control on the Selective, Nonselective, and Absent Response of a Partially Substituted Lower Rim Calix[4]Arene Derivative for Soft Metal Cations (Mercury(II) and Silver(I)). Structural and Thermodynamic Studies. *J. Phys. Chem. A* **2005**, *109*, 6743–6751. [CrossRef] [PubMed]
42. Horvat, G.; Stilinović, V.; Kaitner, B.; Frkanec, L.; Tomišić, V. The Effect of Specific Solvent-Solute Interactions on Complexation of Alkali-Metal Cations by a Lower-Rim Calix[4]Arene Amide Derivative. *Inorg. Chem.* **2013**, *52*, 12702–12712. [CrossRef] [PubMed]
43. Požar, J.; Nikšić-Franjić, I.; Cvetnić, M.; Leko, K.; Cindro, N.; Pičuljan, K.; Borilović, I.; Frkanec, L.; Tomišić, V. Solvation Effect on Complexation of Alkali Metal Cations by a Calix[4]Arene Ketone Derivative. *J. Phys. Chem. B* **2017**, *121*, 8539–8550. [CrossRef] [PubMed]
44. Horvat, G.; Frkanec, L.; Cindro, N.; Tomišić, V. A Comprehensive Study of the Complexation of Alkali Metal Cations by Lower Rim Calix[4]Arene Amide Derivatives. *Phys. Chem. Chem. Phys.* **2017**, *19*, 24316–24329. [CrossRef] [PubMed]
45. Leko, K.; Usenik, A.; Cindro, N.; Modrušan, M.; Požar, J.; Horvat, G.; Stilinović, V.; Hrenar, T.; Tomišić, V. Enhancing the Cation-Binding Ability of Fluorescent Calixarene Derivatives: Structural, Thermodynamic, and Computational Studies. *ACS Omega* **2023**, *8*, 43074–43087. [CrossRef] [PubMed]
46. Arnaud-Neu, F.; Collins, E.M.; Deasy, M.; Ferguson, G.; Harris, S.J.; Kaitner, B.; Lough, A.J.; McKervey, M.A.; Marques, E. Synthesis, X-Ray Crystal Structures, and Cation-Binding Properties of Alkyl Calixaryl Esters and Ketones, a New Family of Macrocyclic Molecular Receptors. *J. Am. Chem. Soc.* **1989**, *111*, 8681–8691. [CrossRef]
47. Śliwa, W.; Girek, T. Calixarene Complexes with Metal Ions. *J. Incl. Phenom. Macrocycl. Chem.* **2010**, *66*, 15–41. [CrossRef]
48. Horvat, G.; Stilinović, V.; Hrenar, T.; Kaitner, B.; Frkanec, L.; Tomišić, V. An Integrated Approach (Thermodynamic, Structural, and Computational) to the Study of Complexation of Alkali-Metal Cations by a Lower-Rim Calix[4]Arene Amide Derivative in Acetonitrile. *Inorg. Chem.* **2012**, *51*, 6264–6278. [CrossRef] [PubMed]
49. Danil de Namor, A.F.; Matsufuji-Yasuda, T.T.; Zegarra-Fernandez, K.; Webb, O.A.; El Gamouz, A. An Enchiridion of Supramolecular Thermodynamics: Calix[*N*]Arene (*N* = 4,5,6) Tertiary Amide Derivatives and Their Ionic Recognition. *Croat. Chem. Acta* **2013**, *86*, 1–19. [CrossRef]
50. Gutsche, C.D.; Bauer, L.J. Calixarenes. 13. The Conformational Properties of Calix[4]Arenes, Calix[6]Arenes, Calix[8]Arenes, and Oxacalixarenes. *J. Am. Chem. Soc.* **1985**, *107*, 6052–6059. [CrossRef]
51. Ikeda, A.; Shinkai, S. Novel Cavity Design Using Calix[*n*]Arene Skeletons: Toward Molecular Recognition and Metal Binding. *Chem. Rev.* **1997**, *97*, 1713–1734. [CrossRef] [PubMed]
52. Meier, U.C.; Detellier, C. Complexation of the Caesium Cation by the Host *p-tert*-Butylcalix[6]Arene Hexaacetamide. *Dalton Trans.* **2003**, *32*, 4574–4579. [CrossRef]
53. Meier, U.; Detellier, C. Complexation of the Sodium Cation by a Calix[8]Arene Derivative: Formation of 2:1 and 3:1 Na+-Calixarene Complexes in Solution. *Supramol. Chem.* **1998**, *9*, 289–295. [CrossRef]
54. Schalley, C.A. *Analytical Methods in Supramolecular Chemistry*, 2nd ed.; John Wiley & Sons, Incorporated: Somerset, NJ, USA, 2012.
55. Tranfić Bakić, M.; Klarić, D.; Espinosa, M.S.; Kazazić, S.; Frkanec, L.; Babay, P.A.; Galić, N. Syntheses of Ester and Amide Derivatives of Calix[6]Arene and Their Complexation Affinities towards La^{3+}, Eu^{3+}, and Yb^{3+}. *Supramol. Chem.* **2019**, *31*, 723–731. [CrossRef]
56. Fanni, S.; Arnaud-Neu, F.; McKervey, M.A.; Schwing-Weill, M.J.; Ziat, K. Dramatic Effects of *p*-Dealkylation on the Binding Abilities of *p*-Tert-Butylcalix[6]Arenes: New Cs^{+} and Sr^{2+} Selective Receptors. *Tetrahedron Lett.* **1996**, *37*, 7975–7978. [CrossRef]
57. Gans, P.; Sabatini, A.; Vacca, A. Investigation of Equilibria in Solution. Determination of Equilibrium Constants with the HYPERQUAD Suite of Programs. *Talanta* **1996**, *43*, 1739–1753. [CrossRef] [PubMed]
58. Chen, R.F. Measurements of Absolute Values in Biochemical Fluorescence Spectroscopy. *J. Res. Natl. Bur. Stand. Sect. Phys. Chem.* **1972**, *76A*, 593. [CrossRef] [PubMed]
59. Crosby, G.A.; Demas, J.N. Measurement of Photoluminescence Quantum Yields. Review. *J. Phys. Chem.* **1971**, *75*, 991–1024. [CrossRef]
60. Resch-Genger, U.; Rurack, K. Determination of the Photoluminescence Quantum Yield of Dilute Dye Solutions (IUPAC Technical Report). *Pure Appl. Chem.* **2013**, *85*, 2005–2013. [CrossRef]
61. Würth, C.; Grabolle, M.; Pauli, J.; Spieles, M.; Resch-Genger, U. Relative and Absolute Determination of Fluorescence Quantum Yields of Transparent Samples. *Nat. Protoc.* **2013**, *8*, 1535–1550. [CrossRef] [PubMed]
62. Brouwer, A.M. Standards for Photoluminescence Quantum Yield Measurements in Solution (IUPAC Technical Report). *Pure Appl. Chem.* **2011**, *83*, 2213–2228. [CrossRef]
63. Riddick, J.A.; Bunger, W.B.; Sakano, T.; Weissberger, A. *Organic Solvents: Physical Properties and Methods of Purification*, 4th ed.; Techniques of Chemistry; Wiley: New York, NY, USA, 1986.
64. Montalti, M.; Credi, A.; Prodi, L.; Gandolfi, M.T. *Handbook of Photochemistry*; CRC Press: Boca Raton, FL, USA, 2006.
65. Dang, V.Q.; Teets, T.S. A Practical Guide to Measuring and Reporting Photophysical Data. *Dalton Trans.* **2025**, *54*, 16268–16284. [CrossRef] [PubMed]

66. Gans, P.; Sabatini, A.; Vacca, A. Simultaneous Calculation of Equilibrium Constants and Standard Formation Enthalpies from Calorimetric Data for Systems with Multiple Equilibria in Solution. *J. Solut. Chem.* **2008**, *37*, 467–476. [CrossRef]
67. Berendsen, H.J.C.; van der Spoel, D.; van Drunen, R. GROMACS: A Message-Passing Parallel Molecular Dynamics Implementation. *Comput. Phys. Commun.* **1995**, *91*, 43–56. [CrossRef]
68. Lindahl, E.; Hess, B.; van der Spoel, D. GROMACS 3.0: A Package for Molecular Simulation and Trajectory Analysis. *J. Mol. Model.* **2001**, *7*, 306–317. [CrossRef]
69. van der Spoel, D.; Lindahl, E.; Hess, B.; Groenhof, G.; Mark, A.E.; Berendsen, H.J.C. GROMACS: Fast, Flexible, and Free. *J. Comput. Chem.* **2005**, *26*, 1701–1718. [CrossRef] [PubMed]
70. Hess, B.; Kutzner, C.; van der Spoel, D.; Lindahl, E. GROMACS 4: Algorithms for Highly Efficient, Load-Balanced, and Scalable Molecular Simulation. *J. Chem. Theory Comput.* **2008**, *4*, 435–447. [CrossRef] [PubMed]
71. Pronk, S.; Páll, S.; Schulz, R.; Larsson, P.; Bjelkmar, P.; Apostolov, R.; Shirts, M.R.; Smith, J.C.; Kasson, P.M.; van der Spoel, D.; et al. GROMACS 4.5: A High-Throughput and Highly Parallel Open Source Molecular Simulation Toolkit. *Bioinformatics* **2013**, *29*, 845–854. [CrossRef] [PubMed]
72. Abraham, M.J.; Murtola, T.; Schulz, R.; Páll, S.; Smith, J.C.; Hess, B.; Lindahl, E. GROMACS: High Performance Molecular Simulations through Multi-Level Parallelism from Laptops to Supercomputers. *SoftwareX* **2015**, *1–2*, 19–25. [CrossRef]
73. Best, R.B.; Zhu, X.; Shim, J.; Lopes, P.E.M.; Mittal, J.; Feig, M.; MacKerell, A.D. Optimization of the Additive CHARMM All-Atom Protein Force Field Targeting Improved Sampling of the Backbone ϕ, ψ and Side-Chain χ_1 and χ_2 Dihedral Angles. *J. Chem. Theory Comput.* **2012**, *8*, 3257–3273. [CrossRef] [PubMed]
74. Bussi, G.; Donadio, D.; Parrinello, M. Canonical Sampling through Velocity Rescaling. *J. Chem. Phys.* **2007**, *126*, 014101. [CrossRef] [PubMed]
75. Bernetti, M.; Bussi, G. Pressure Control Using Stochastic Cell Rescaling. *J. Chem. Phys.* **2020**, *153*, 114107. [CrossRef] [PubMed]
76. Swope, W.C.; Andersen, H.C.; Berens, P.H.; Wilson, K.R. A Computer Simulation Method for the Calculation of Equilibrium Constants for the Formation of Physical Clusters of Molecules: Application to Small Water Clusters. *J. Chem. Phys.* **1982**, *76*, 637–649. [CrossRef]
77. Darden, T.; York, D.; Pedersen, L. Particle Mesh Ewald: An $N\cdot\log(N)$ Method for Ewald Sums in Large Systems. *J. Chem. Phys.* **1993**, *98*, 10089–10092. [CrossRef]
78. Humphrey, W.; Dalke, A.; Schulten, K. VMD: Visual Molecular Dynamics. *J. Mol. Graph.* **1996**, *14*, 33–38. [CrossRef] [PubMed]
79. Casnati, A.; Baldini, L.; Pelizzi, N.; Rissanen, K.; Ugozzoli, F.; Ungaro, R. Strontium Complexes of Calixarene Amides in the Solid State: Structural Dependence on the Ligand Size and on the Counter Ions. *J. Chem. Soc. Dalton Trans.* **2000**, *29*, 3411–3415. [CrossRef]
80. Casnati, A.; Minari, P.; Pochini, A.; Ungaro, R.; Nijenhuis, W.F.; De Jong, F.; Reinhoudt, D.N. Selective Complexation and Membrane Transport of Guanidinium Salts by Calix[6]Arene Amides. *Isr. J. Chem.* **1992**, *32*, 79–87. [CrossRef]

Disclaimer/Publisher's Note: The statements, opinions and data contained in all publications are solely those of the individual author(s) and contributor(s) and not of MDPI and/or the editor(s). MDPI and/or the editor(s) disclaim responsibility for any injury to people or property resulting from any ideas, methods, instructions or products referred to in the content.